Electronic Supplementary Information (ESI)

Closing the Loop in Nanotheranostics: From ^{124}I Separation to Intrinsically Radiolabeled Platinum Nanoparticles for Potential PET/CT-Guided Photothermal Therapy

Sanchita Ghosh,[1,2] Rajwardhan N. Ambade,[1] Ramu Ram,[1] Kanhu C Barick,[3,2] Apurav Guleria,[4,2] Suresh Chand Sharma,[5] Minati Nayak,[4,2] Amit Kunwar,[4,2] Kaustava Bhattacharyya,[3,2] Rubel Chakravarty[1,2,*]

[1]Radiopharmaceuticals Division, Bhabha Atomic Research Centre, Trombay, Mumbai, 400085, India

[2]Homi Bhabha National Institute, Anushaktinagar, Mumbai, 400094, India

[3]Chemistry Division, Bhabha Atomic Research Centre, Trombay, Mumbai, 400085, India

[4]Radiation and Photochemistry Division, Bhabha Atomic Research Centre, Trombay, Mumbai, 400085, India

[5]Nuclear Physics Division, Bhabha Atomic Research Centre, Trombay, Mumbai, 400085, India

To whom all correspondences must be addressed:

Rubel Chakravarty, Ph.D.

E-mail: rubelc@barc.gov.in, rubelchakravarty@gmail.com

S1. Materials and Methods

S1.1 Materials

Chloroplatinic acid hexahydrate ($H_2PtCl_6 \cdot H_2O$), sodium borohydride ($NaBH_4$), gum arabic glycoprotein (MW ~250 kDa), tellurium (IV) oxide (TeO_2, ≥99%) and all other chemicals were obtained from Sigma-Aldrich and used as received. PD-10 columns were purchased from GE Healthcare. All solutions were prepared using Milli-Q water.

S1.2 Production and Radiochemical Separation of ^{124}I

^{124}I was produced via the ^{124}Te (p,n) ^{124}I nuclear reaction by proton irradiation of natural TeO_2 targets. Briefly, 50 mg of natural TeO_2 was pressed into a pellet (5 mm diameter, ~100 μm thickness) using a hydraulic press (25 kN cm^{-2}). The pellet was wrapped in aluminum foil (0.0254 mm) to prevent sputtering during irradiation. The target was irradiated at the BARC–TIFR Pelletron facility using a 14 MeV proton beam at a current of 150 nA, followed by a cooling period of 4 h prior to handling.

The irradiated target was dissolved in 0.1 M NaOH and subjected to chromatographic separation using mesoporous alumina.[1] For this, 200 mg of mesoporous alumina was packed into a glass column (3 mm × 60 mm) and preconditioned to pH ~6. The radioactive solution was passed through the column at a flow rate of 0.25 mL min^{-1}, under which conditions radioiodine was selectively retained. The column was subsequently washed with water to remove residual impurities, and ^{124}I was eluted using 2 mL of 0.01 M NaOH.

Radionuclidic purity of the separated sample was evaluated by gamma spectrometry using an HPGe detector coupled to a multichannel analyzer. The efficiency and selectivity of the separation process were evaluated by ICP-AES analysis of the decayed samples.

S1.3 Synthesis of Pt@GA Nanoparticles

Pt@GA NPs were synthesized by reducing H_2PtCl_6 (5 mg) in an aqueous gum arabic solution (10 mg in 4 mL). Ice-cold $NaBH_4$ (1 mL, 1 M) was added, and the reaction mixture was stirred for 2 h until a color change from yellow to black was observed.

S1.4 Characterization Techniques

The hydrodynamic diameter of the NPs was determined using dynamic light scattering (DLS) in a Microtrac Series MN420 – Nanotrac Wave II particle analyzer (Germany). The colloidal stability and relaxation time of the Pt@GA NPs were evaluated using Xigo Nanotools Acorn Area instrument. To verify the formation of the NPs, UV-Visible absorption spectra were recorded using a JASCO UV-Vis spectrophotometer (Japan). High-resolution transmission electron microscopy (HRTEM) images of the NPs were obtained using a Field Emission Gun-Transmission Electron Microscope (FEG-TEM) system operating at 120/200 kV (JEM 2100F model, JEOL, USA). The powdered form of the NPs was obtained by freeze drying the NPs formulation in Martin Christ lyophilizer (Germany). The X-ray diffraction (XRD) pattern of the powdered NPs was measured using a Phillips PW1710 diffractometer. Raman spectra of the NPs were recorded using a Seki STR300 Raman spectrometer. The bonding characteristics of the NPs were investigated by analyzing their electronic states through X-Ray Photoelectron Spectroscopy (XPS) using a SPECS system equipped with a PHOBIOS 150 Delay Line Detector (DLD). An Al K_α (1483.6 eV) dual anode was used as the X-ray source of power 250 W, 13 kV voltage and 175.6 nA sample current, at a pass energy of 50 eV. The C-1s peak (284.5 eV) was employed as an internal reference for determining the absolute binding energy. Peak deconvolutions were carried out using CASA software, applying a Voigt profile with a GL (30) setting, without introducing asymmetry. The baseline was corrected using the Shirley function. Furthermore, thermogravimetric analysis (TGA) was conducted to evaluate the extent of GA coating on the

surface of Pt NPS using a Mettler Toledo STARe instrument. The sample was heated at a rate of 15 °C min^{-1} in an alumina crucible under a nitrogen gas flow (50 mL min^{-1}).

S1.5 Photothermal Measurements

In this experiment, 1 mL of Pt@GA NPs solutions at varying concentrations (0.25 mg/mL to 1 mg/mL) were placed in a quartz cuvette and exposed to an 808 nm laser (808-LM-2000T) at three different power levels (0.54 W, 0.68 W, 0.81 W). The laser beam had an exposure diameter of 0.6 cm and was applied for 5 minutes, with the distance between the cuvette and the laser source maintained at 2 cm. To assess the photostability, the formulation of Pt@GA NPs was exposed to an 808 nm near-infrared (NIR) laser for five cycles (heating and cooling curve). The temperature change during the irradiation was continuously monitored using a high resolution infrared camera (Testo 875-1 Thermal Imager) and analyzed with thermography software (Testo IR Soft Software, version 3.1). Furthermore, a fiber optic signal conditioner (FOTEMP1-H, Micronor Inc., USA) was used to record the temperature changes at different time intervals. Deionized water was used as a control.

S1.6 In Vitro Cell Studies

Human lung adenocarcinoma (A549) cell line was sourced from the National Centre for Cell Sciences, Pune, India. The cells were cultured in Dulbecco's Modified Eagle Medium (DMEM) containing 10% FBS and a penicillin-streptomycin antibiotic mixture (100 U/mL penicillin and 250 µg/mL streptomycin) and maintained in a humidified incubator at 37°C with a 5% CO_2 atmosphere.

To evaluate the cytotoxicity of Pt@GA NPs against A549 cells, 3-[4,5-dimethylthiazol-2-yl]-2,5-diphenyl tetrazolium bromide (MTT) assay was performed. Briefly, A549 cells were seeded at a density of 5 × 10^3 cells per well in a 96-well plate and incubated with different concentrations of Pt@GA NPs. After 48 hours, the culture medium was replaced with 100 µL of MTT reagent (0.5

mg/mL) and incubated for an additional 4 hours at 37°C. The resulting formazan crystals were solubilized by adding 100 µL of solubilizing buffer (10% SDS in water), and the absorbance of the formazan solution was measured at 570 nm using a BioTek Universal Microplate Reader. Cell viability was calculated using the formula: (optical density of treated cells / optical density of control cells) × 100. The results are expressed as mean ± SD (n = 4).

For the evaluation of the photothermal therapy (PTT) of the Pt@GA NPs, in vitro, A549 cells were seeded in a 96-well plate. One group of cells were incubated with 0.25 mg/mL and 0.5 mg/mL Pt@GA NPs for 48 hours, while second group of cells were treated in the same manner but also irradiated with an 808 nm laser at 0.68 W for 5 minutes. A third group of cells were only irradiated with 808 nm laser at 0.68 W for 5 minutes. After 48 hours of treatment, cell viability was determined using the standard MTT assay as discussed above. Cellular morphological changes following treatment were observed and recorded using a bright field microscope.

S1.7 Radiolabeling of Pt@GA NPs with ^{124}I

The solution of Pt@GA NPs (1 mL) was placed in a 10 mL glass vial, and 100 µL of separated ^{124}I (~2.6 MBq) solution was added. The mixture was kept for 30 minutes at room temperature. The radiolabeling efficiency was assessed using size exclusion chromatography with a PD-10 column (G.E. Healthcare).[2] For this, 0.5 mL of the [^{124}I]Pt@GA NPs solution was loaded onto a PBS equilibrated PD-10 column, and the column was subsequently eluted with PBS. The elution profile was obtained by measuring the radioactivity of each 0.5 mL fraction using a NaI (Tl) detector.

Moreover, the radiochemical stability of the ^{124}I labeled Pt@GA NPs was evaluated by incubating the radiolabeled NPs in a tenfold excess volume of PBS and human serum at room temperature, following the procedure previously described by our group.[2]

S1.8 PET Imaging

In order to assess the feasibility of the radiolabeled nanoplatform as a PET imaging agent, in vitro PET imaging of [^{124}I]Pt@GA NPs was conducted at a fixed concentration of 5 mg/mL and varying the amount of radioactivity using a Philips Gemini TF 16-slice PET system (Netherlands).

S1.9 CT imaging

CT scans along with Hounsfield unit (HU) measurements of Pt@GA NPs at five different mass concentrations of Pt@GA NPs were obtained using a GE (model: 670DR) SPECT/CT system.

S2. Additional Discussion

S2.1 Quality control of separated ^{124}I

Radionuclidic purity of the separated sample was evaluated by gamma spectrometry using an HPGe detector coupled to a multichannel analyzer. The spectrum showed characteristic peaks corresponding to ^{124}I (603, 645, and 722 keV), along with minor contributions from co-produced iodine isotopes such as ^{123}I, ^{126}I, and ^{130}I, and the annihilation peak at 511 keV (**Figure S2**). The use of enriched ^{124}Te targets can minimize the formation of extraneous radioisotopes. The present approach demonstrates that high quality ^{124}I suitable for radiopharmaceutical applications can be obtained using natural targets through a simple and robust separation protocol. The efficiency and selectivity of the separation process were further confirmed by ICP-AES analysis of the decayed samples, which showed residual Te levels below 0.01 ppm, indicating effective removal of the target matrix and high chemical purity of the isolated ^{12x}I (x = 123, 124, 126, 130).

The minor co-produced radioisotopes do not alter the chemical behavior of radioiodide and therefore have no impact on labeling efficiency or NP stability. For the in vitro PET imaging studies, their contribution to image interpretation would be negligible. While such impurities may

influence highly quantitative dosimetry, this is not critical for the present proof-of-concept investigation. The use of enriched ^{124}Te targets would substantially reduce the formation of these radioisotopes when higher radionuclidic purity is required.

S2.2 Characterization and colloidal Stability

In this study Pt@GA NPs was synthesized by controlled reduction of chloro platinic acid with $NaBH_4$ in presence of gum arabic glycoprotein. The average hydrodynamic size of the NPs was 22.06 ± 0.15 nm and TEM images revealed smaller, quasi-spherical Pt cores of 4.8 ± 1.4 nm. The substantial difference between the DLS and TEM sizes arises from the distinct physical quantities measured by the two techniques. DLS determines the hydrodynamic diameter of the nanoparticles in aqueous solution, which includes the metallic core, the hydrated gum arabic corona, bound water molecules, and any small reversible aggregates present in dispersion. In contrast, TEM provides the size of the dried electron-dense platinum cores alone. The observed values are therefore fully consistent with a small platinum core stabilized by a substantially larger hydrated bio-polymeric shell. The hydrodynamic diameter was also measured over 7 consecutive days to assess particle size changes over time (**Figure S3**). After 6 days, a slight increase in particle size was observed, indicating a reduction in colloidal stability due to agglomeration of the GA glycoprotein coating on the inorganic NPs surface. This was further confirmed by magnetic T_2 relaxation time measurements (**Figure S4**). The initial T_2 relaxation time for the freshly synthesized nanoformulation was 2539 ± 38 ms. However, a slight decrease was observed on day 10, with the T_2 relaxation time reducing to 2369 ± 46 ms (**Figure S4**).

Figure 1c represents the HRTEM image of Pt@GA NPs. The NPs were observed to self-assemble, likely due to the presence of gum arabic on their surface. The inset in **Figure 1c** shows the selected area electron diffraction (SAED) pattern, confirming the crystalline structure of the NPs. At higher magnification (inset: **Figure 1c**), reveals the fringe pattern, although the boundaries are not clearly defined due to the gum arabic induced self-assembly. Additionally, the

lattice spacing determined from the fringes for (111) plane was found to be ~ 0.22 nm which matches with the face centered cubic phase of Pt (JCPDS no. 87-0636). In addition the shape of the NPs were found to be quasi-spherical, with an average size of 4.8 ± 1.4 nm (**Figure 1c & 2d**).

The crystallinity of the NPs was additionally analyzed through XRD pattern of Pt@GA NPs shown in **Figure S5**, which shows a broad diffuse background arising from the amorphous gum arabic matrix. Nonetheless, the appearance of two main peaks (at 2θ ~ 39.5 and 45.9 degrees) matched with the theoretical values at 39.5 and 45.9 degrees (JCPDS no. 87-0636). This categorically confirms the formation of Pt NPs. However, relatively low intensity and broadness of the Pt peaks are consistent with their small sizes, as observed from the TEM studies.

Thermogravimetric analysis (TGA) of Pt@GA NPs reveals a multistep mass loss pattern, as shown in **Figure S6**. An initial ~ 10% weight loss below 150 °C is attributed to the removal of physisorbed and weakly bound water, consistent with the hygroscopic nature of gum arabic. A second major loss of ~ 20% between 180 and 350 °C probably corresponds to the thermal degradation of the organic polymer chains components of gum arabic. This decomposition interval agrees well with literature establishing 250–300 °C as the principal degradation region for gum arabic.[3-5] A third, broader mass-loss step of ~ 7% from ~350 to 500 °C could be attributed to the degradation of the residual polymer content. Above 600 °C, the mass stabilizes with a final residue of ~ 60%, corresponding to the inorganic fraction dominated by metallic Pt together with trace mineral components naturally present in gum arabic. Overall, the TGA profile confirms the successful formation of Pt NPs coated by gum arabic matrix.

UV–vis spectra of Pt@GA NPs is shown in **Figure S7**. The formation of Pt@GA NPs is evident from their spectral profile extending from the UV to the near-infrared. Similar spectral profiles of Pt NPs have been reported by other researchers.[6-9] It can be seen that the absorption spectrum of Pt@GA NPs lacks the sharp, distinct peaks in the visible region that are characteristic

of strong surface plasmon resonance in some other noble metals. Such broad featureless profile could be attributed to their unique electronic band structure, which results in heavily damped surface plasmon resonances and the location of characteristic absorption features in the UV region.

The composition of the synthesized NPs was analyzed using XPS. **Figure S8a** displays the survey spectrum, while the core-level XPS spectra of Pt 4f and O 1s are shown in **Figures S8b** and **S8c**, respectively. The Pt 4f spectrum of the synthesized NPs exhibited spin -orbit splitting with two peaks found at $4f_{7/2}$ and $4f_{5/2}$ with the spin-orbit splitting parameter (Δε) of 3.33 eV as has been shown earlier in the literature.[10] The Pt-$4f_{7/2}$ has a binding energy of 70.5 eV which corroborates components, characteristic of metallic platinum.[10, 11] The deconvoluted O 1s XPS-spectra revealed two peaks at binding energies of 529.5 eV and 531.2 eV. The O-1s at 531.2 eV is generically represented for the surface -OH group. Every surface definitely ends with a surface -OH group and this peak represents the same.[12, 13] As the Pt is found in the metallic state the other peak O is not attached with the Pt metal. The other probability is the O-from the protein, however the O-1s representing the protein usually are found at >531 eV as these O are strongly bound to other molecules. Therefore, this O-1s is mostly for the surface physisorbed O over the Pt -metal which is usually found at ~ 530 EV in this case 529.5 eV.[14]

S2.4 Photothermal conversion efficiency calculation

As reported by Roper et al., the energy balance of the entire system is represented by[15]

$$\sum_i m_i\, c_{p,i}\, dTdt = Q_{NP} + Q_{Dis} - Q_{surr} \quad \text{.....(1)}$$

where m and c_p are the mass and specific heat capacity of the dispersing medium (i.e., water), T is temperature of the system and t represent time.

The heat inputted by sample on laser irradiation is given by the term Q_{NP}. Under irradiation of NIR laser light (808 nm), heat is dissipated from the surface of Pt-GA NPs by the plasmonic resonance and it is given by:

$Q_{NP} = (1 - 10^{-A808})$ .....(2)

where I represent incident laser power, η is the photothermal conversion efficiency from the laser irradiation energy to thermal energy, and A_{808} is the absorbance of the Pt-GA NPs.

The term Q_{Dis} expresses heat dissipated from light absorbed by quartz cell itself, and it was measured independently to be 31 mW in quartz cell containing pure water without Pt-GA NPs. Furthermore, Q_{Surr} is the heat conduction away from the sample surface by air. It is linear with temperature for the outgoing thermal energy, as given by Eq. 3:

$Q_{Surr} = hS\ (T - TS_{urr})$ .....(3)

where h is heat transfer coefficient, S is the surface area of the container, T temperature of the system surface and T_{Surr} is ambient temperature of the surroundings.

With the defined laser power, the heat input ($Q_{NP} + Q_{Dis}$) will become finite. Since the heat output (Q_{Surr}) is increased along with the increase of the temperature according to the Eq. 3, the system reaches to maximum temperature, when the heat input is equal to heat output:

$Q_{NP} + Q_{Dis} = Q_{Surr\text{-}Max} = hS\ (T_{Max} - T_{Surr})$ .....(4)

where the $Q_{Surr\text{-}Max}$ is heat conduction away from the system surface by air when the sample cell reaches the equilibrium temperature, and T_{max} is the equilibrium temperature. Thus, NIR laser heat conversion efficiency (η) can be determined by substituting Eq. 2 for Q_{NP} into Eq. 4 and rearranging to get

$$\eta = \frac{hS\left(T_{Max} - T_{Surr}\right) - Q_{Dis}}{I\left(1 - 10^{-A_{808}}\right)} \qquad \text{.....(5)}$$

The maximum steady temperature (T_{max}) of the solution of the Pt-GA NPs was 43.4°C and environmental temperature (T_{Surr}) was 27.3°C. So, the temperature change (T_{Max}-T_{Surr}) of the solution of the Pt-GA NPs 16.8°C. The laser power I is 0.68 W. The absorbance of the Pt-GA NPs at 808 nm (A_{808}) is 0.552 (obtained after baseline correction) for 0.5 mg/ml Pt-GA NPs.

To gain hS, a dimensionless parameter θ is introduced as followed:

$$\theta = \frac{T - T_{Surr}}{T_{Max} - T_{Surr}} \quad \text{.....(6)}$$

A sample system time constant can be calculated as followed:

t = - $\tau_s$ln (θ) .....(7)

According to **Figure S11**, was determined and calculated to be 168.82 s.

τ_s = mC/hS .....(8)

In addition, m is 1g and C is 4.2 J/g·°C. Thus, according to Eq. 7 and 8, hS is deduced to be 24.8 mW/°C. Thus, substituting according values of each parameter to Eq. 5, the photothermal conversion efficiency (η) of the Pt-GA NPs can be calculated to be ~78.7 % under 808 nm NIR light (laser power 0.68 W).

S2.4 Radiolabeling Stability

In this study, Pt@GA NPs was radiolabeled with via intrinsic radiolabeling method.[16] This technique provides a quicker and more straightforward approach to radiolabeling while maintaining the functional properties of the NPs. It is well-established that the adsorption of halide ions onto noble metal surfaces follows a specific order, namely: F^- < Cl^- < Br^- < I^-, with iodide forming a covalent bond with noble metal surface.[17] Given this, it is plausible to hypothesize that iodine would behave similarly, forming a strong chemisorptive bond on the Pt surface through charge-transfer interactions with surface platinum atoms. Although the platinum cores are coated

with gum arabic, this polysaccharide-protein matrix forms a hydrated and porous shell rather than a compact barrier. Consequently, iodide ions can readily diffuse through the coating and access the underlying platinum surface, enabling efficient intrinsic radiolabeling. Accordingly, simple incubation with separated ^{124}I resulted in efficient labeling with radiochemical yields consistently above 99%, as confirmed by size exclusion chromatography (**Figure S13**).[2] This finding affirms that robust binding can occur between noble metals and heavy halide ions, which facilitates stable radiolabeling of Pt@GA NPs with ^{124}I.

The stability of the ^{124}I labeled Pt@GA NPs was also assessed in both PBS and human serum over a period of 7 days. As anticipated, the radiolabeled NPs exhibited excellent stability in both media. In human serum, the radiochemical stability was found to be 94.1 ± 0.7% (n = 3), and in PBS, it was 95.6 ± 0.3% (n = 3), even after 7 days (**Figure S14**). These results confirm that the [^{124}I]Pt@GA NPs maintain their structural integrity in both PBS and serum, making them suitable for potential in vivo applications.

The strong interaction between iodide and platinum is attributed to chemisorption involving charge transfer from iodide to surface platinum atoms, resulting in a stable Pt–I bond. Although the platinum cores are coated with gum arabic, this polysaccharide-protein matrix forms a hydrated and porous shell rather than a compact barrier. Consequently, iodide ions can readily diffuse through the coating and access the underlying platinum surface, enabling efficient intrinsic radiolabeling. The very high radiolabeling yield and prolonged stability in PBS and serum provide experimental evidence that the gum arabic coating does not hinder Pt–I bond formation.

S3. Supplementary Figures

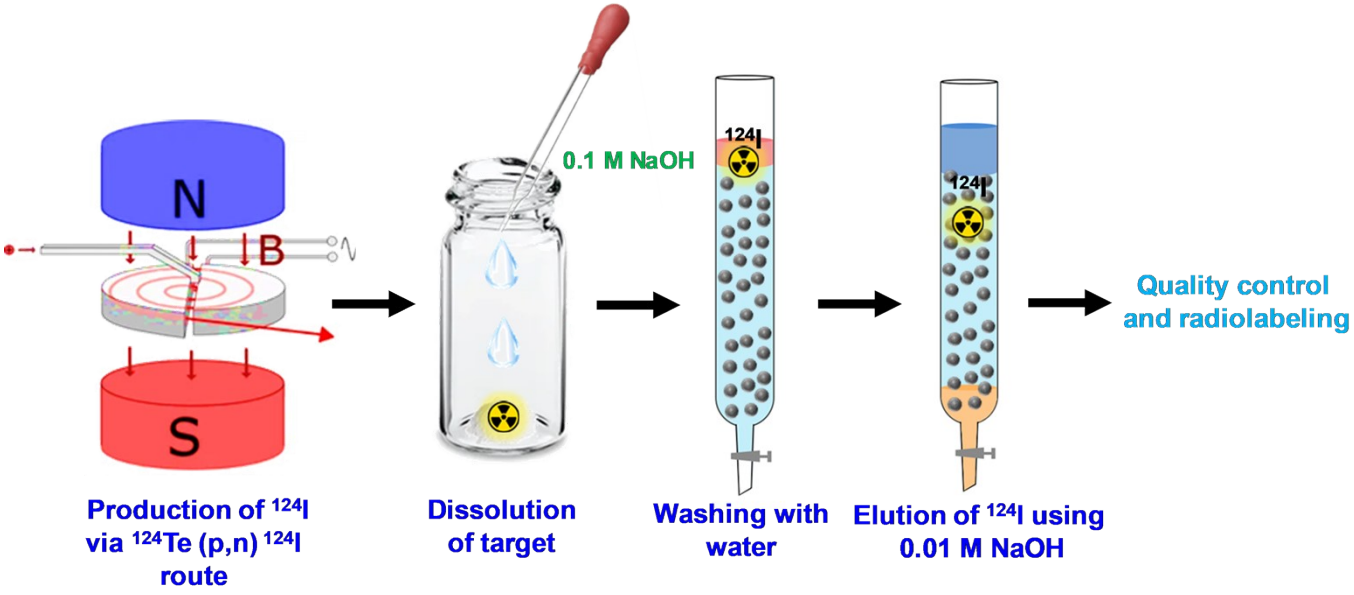

Figure S1. Schematic illustration of production and separation of ^{124}I.

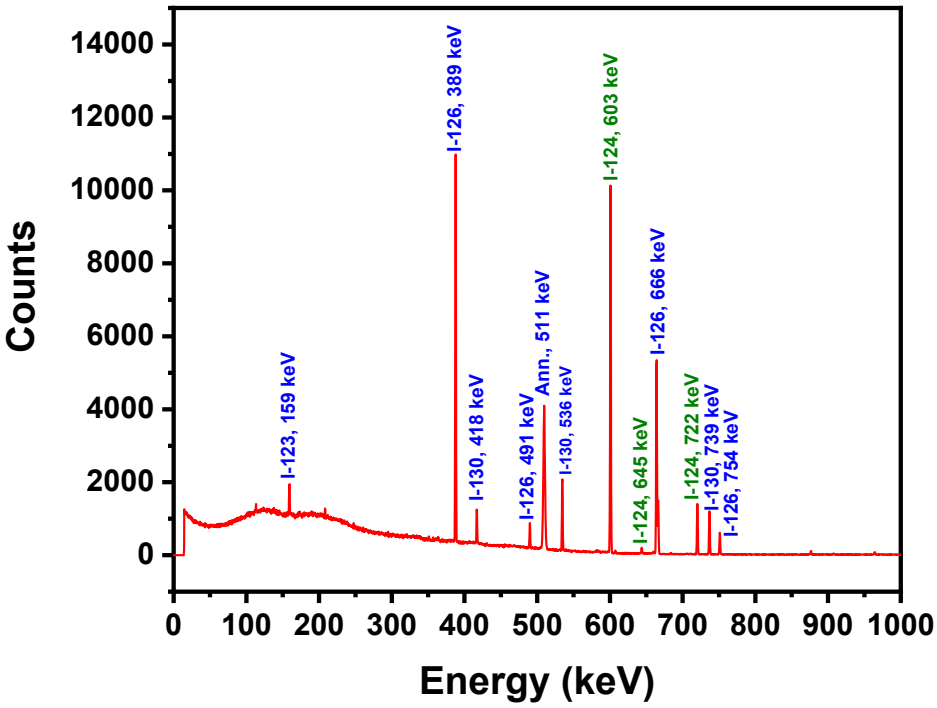

Figure S2. Gamma ray spectrum of ^{124}I after separation.

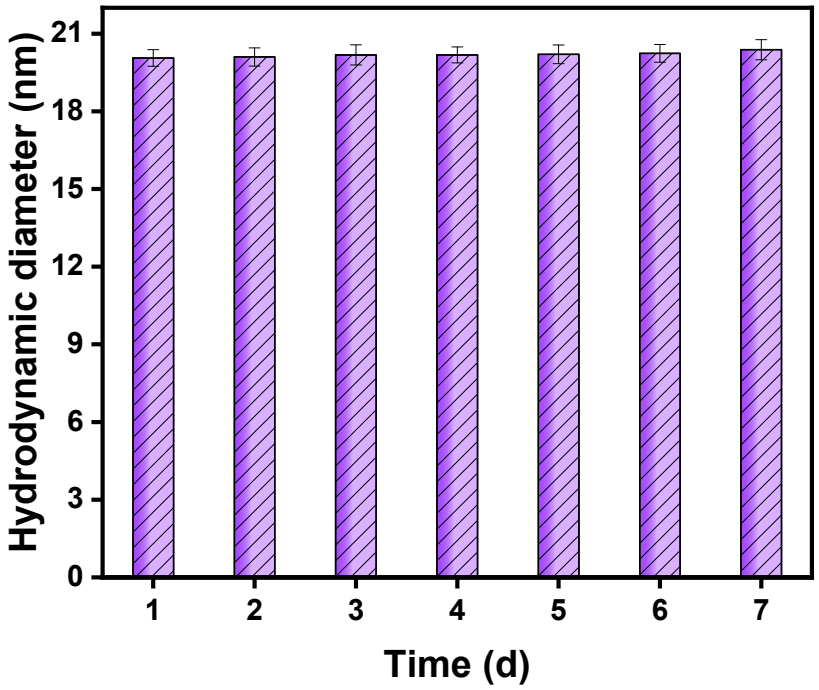

Figure S3. Time dependent variation in hydrodynamic diameter of Pt@GA NPs over 7 days.

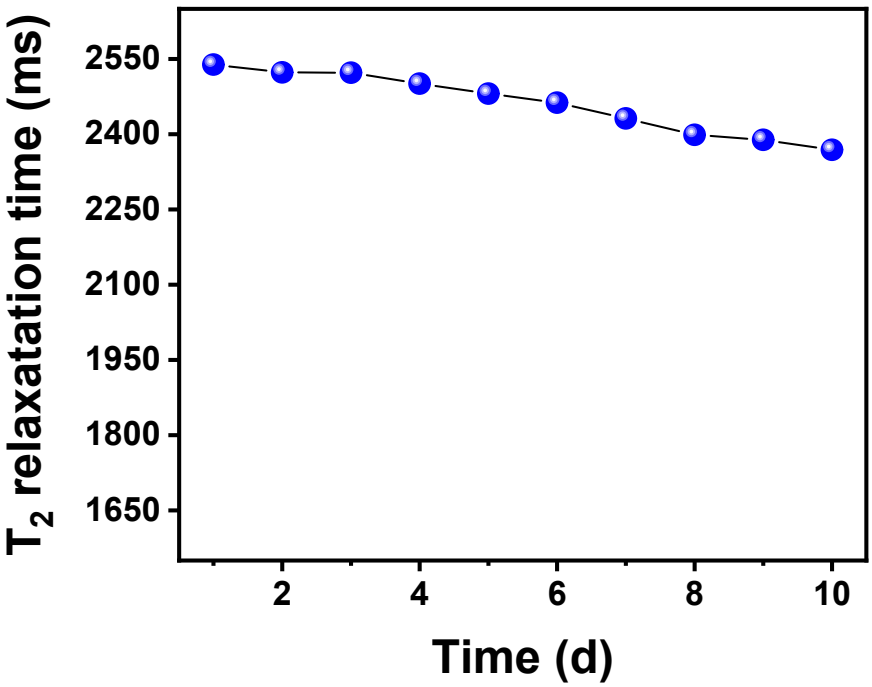

Figure S4. Colloidal stability plot of Pt@GA NPs over a period of 10 days.

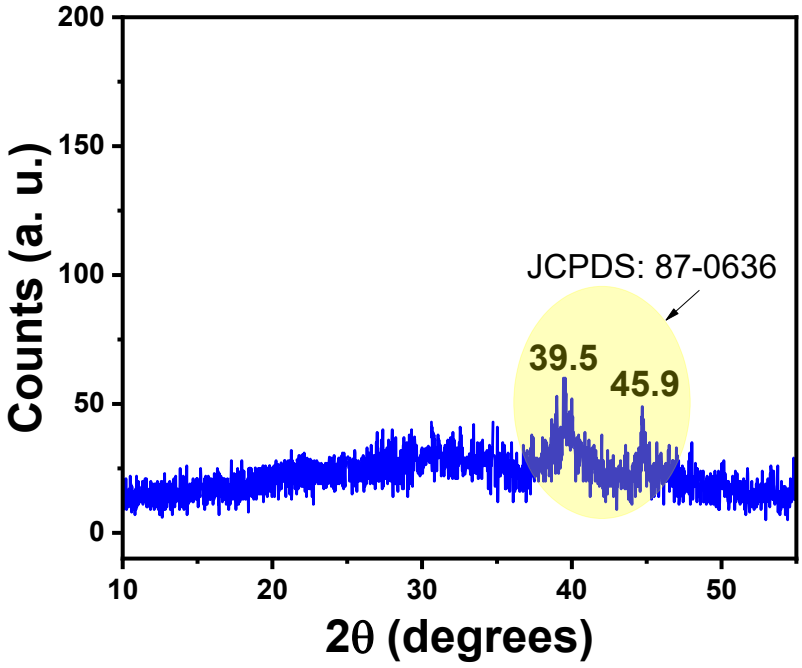

Figure S5. XRD pattern of Pt@GA NPs.

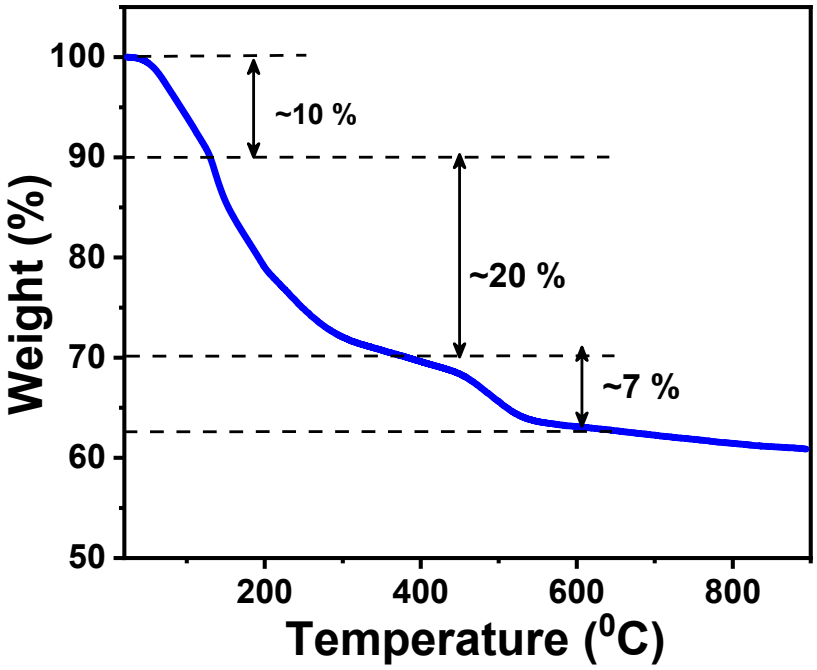

Figure S6. TGA analysis of the Pt@GA NPs.

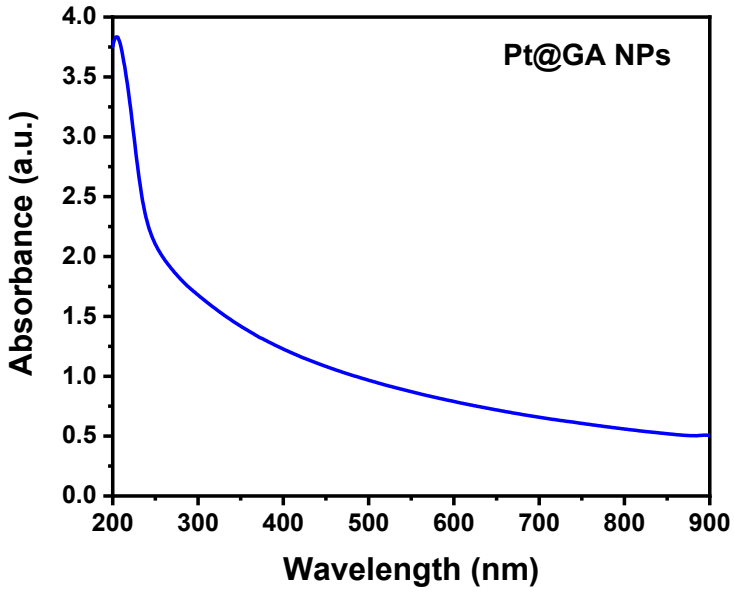

Figure S7. UV-Vis absorption spectra of Pt@GA NPs.

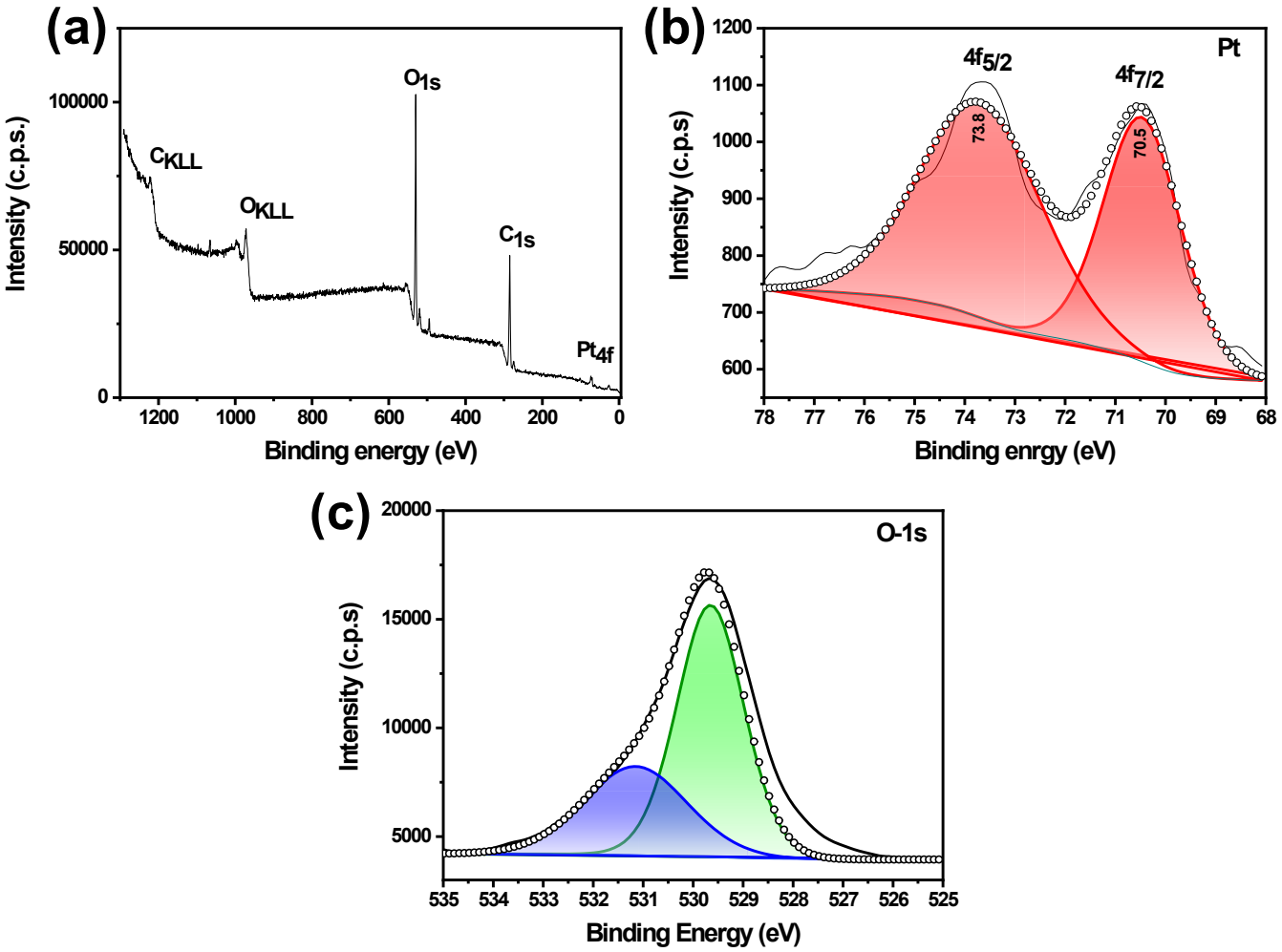

Figure S8. a) Survey spectrum of Pt@GA NPs. Core level XPS spectra of b) Pt 4f and c) O 1s in Pt-GA NPs.

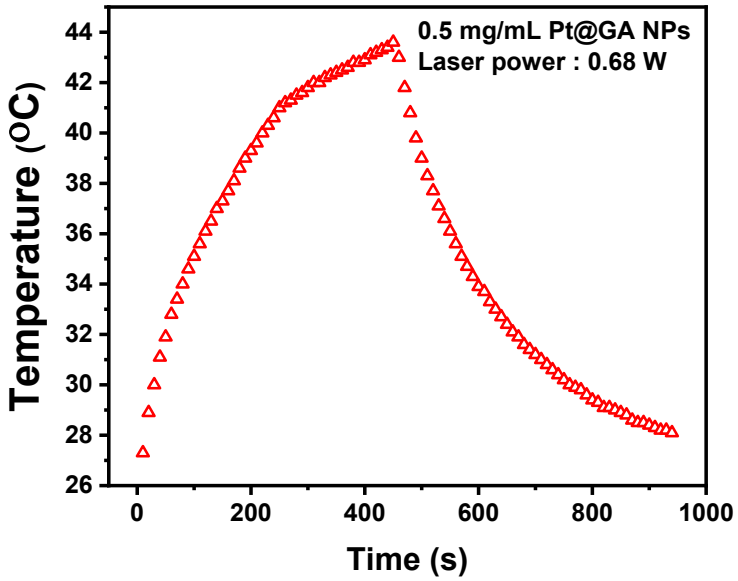

Figure S9. Heating and cooling curve of 0.5 mg/mL of Pt@GA NPs under 808 nm laser irradiation at power of 0.68 W.

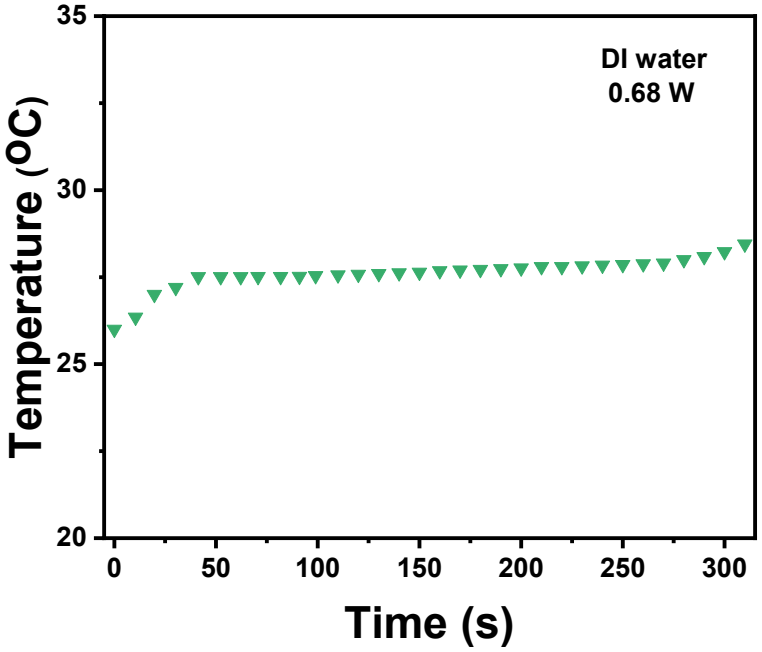

Figure S10. Control heating curve of deionized water under 808 nm laser irradiation.

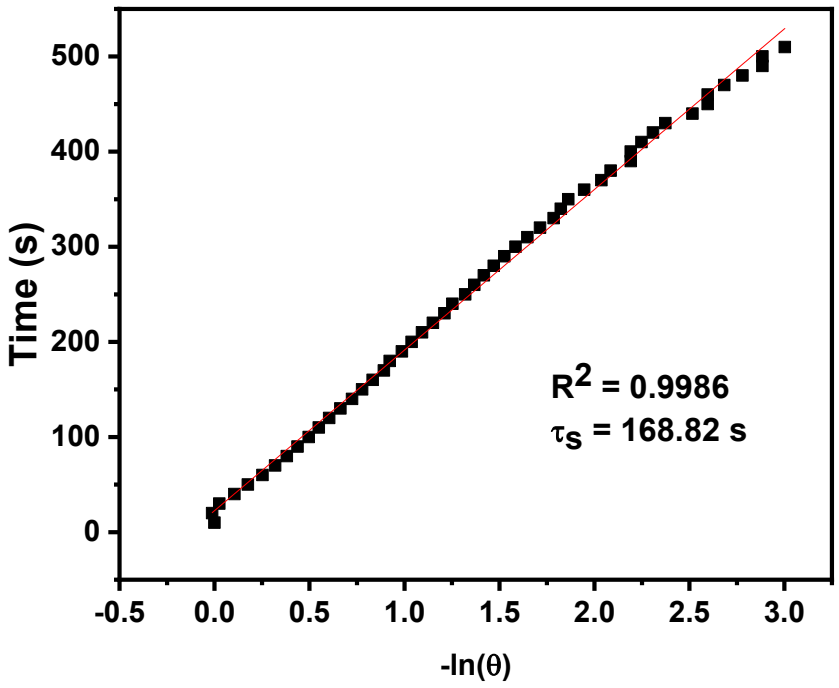

Figure S11. Linear time data of cooling curve vs. negative natural logarithm of θ of Pt@GA NPs.

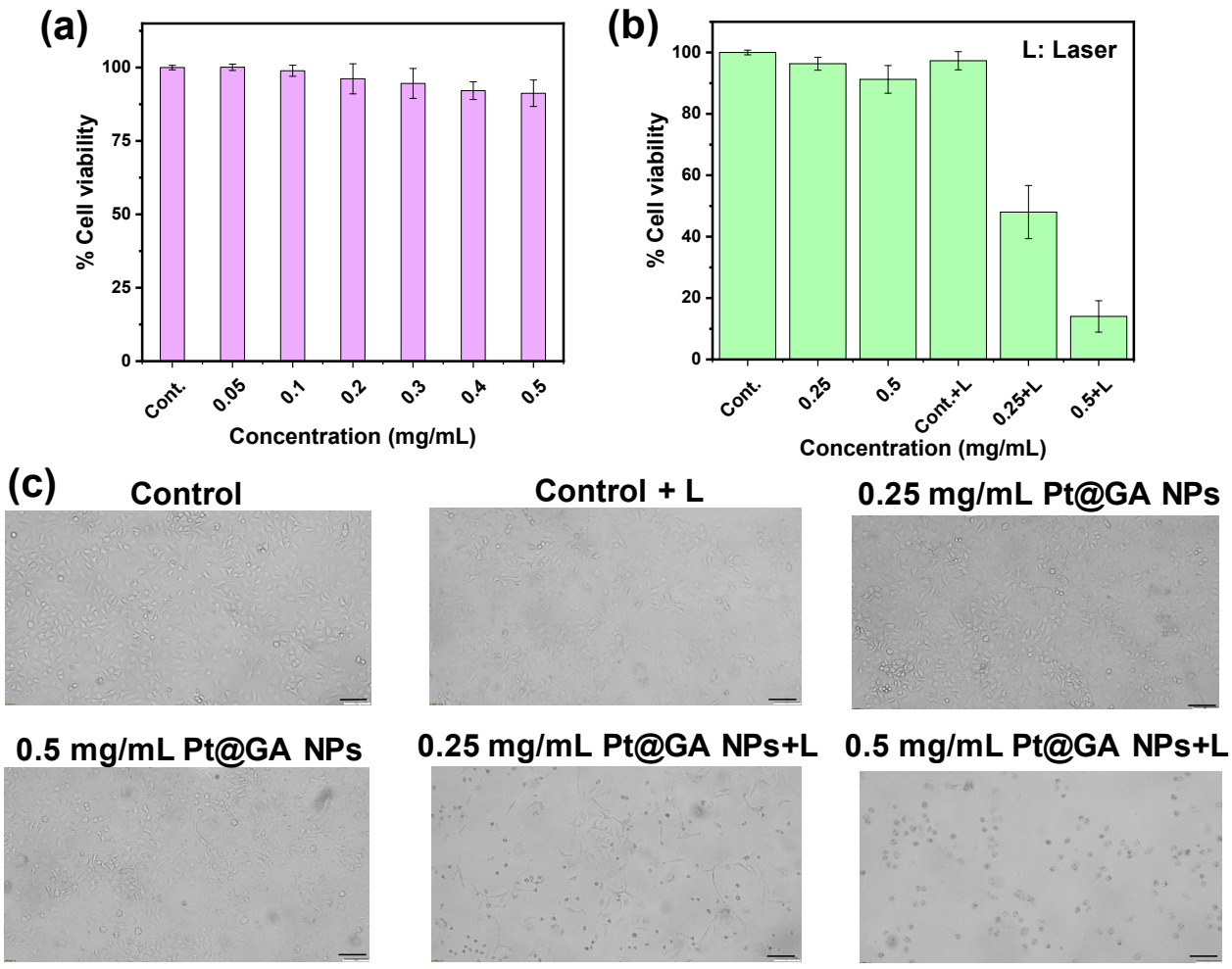

Figure S12. a) Percentage cell viability plot of A549 cell lines upon incubation with different concentration of Pt@GA NPs for 48 hours at 37 °C. b) In vitro photothermal therapeutic effect of 0.25 mg/mL and 0.5 mg/mL of Pt@GA NPs in A549 cell line. The cells treated with Pt@GA NPs were exposed to NIR (808 nm) light for 5 minutes and then cultured for 48 hours prior to MTT assay. Data are shown as mean ± SD (n = 4). c) Bright field microscopy images of A549 cells under various treatment conditions. (L : laser).

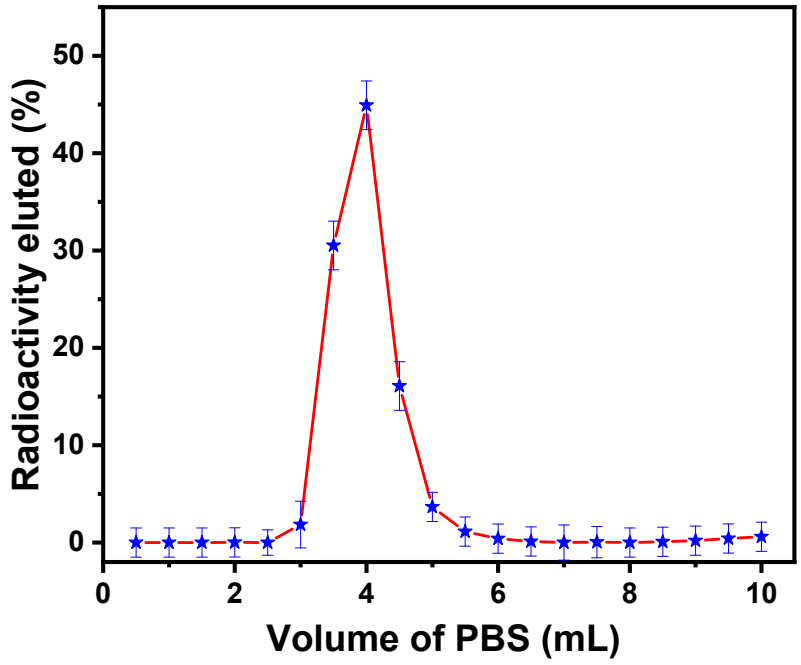

Figure S13. Elution profile of [^{124}I]Pt@GA NPs was obtained through size exclusion chromatography using a PD-10 column (n = 3).

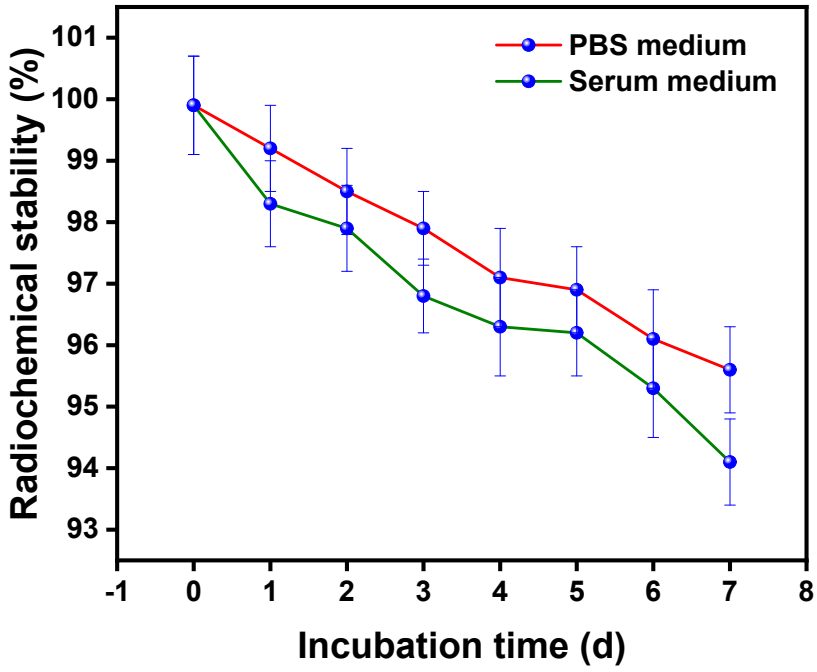

Figure S14. Variation in radiochemical stability of [^{124}I]Pt@GA NPs with time in PBS and serum media.

References

1. R. Chakravarty, J. Bahadur, S. Lohar, H. D. Sarma, D. Sen, R. Mishra, S. Chakraborty and A. Dash, Microporous and Mesoporous Materials, 2019, 287, 271-279.
2. S. Ghosh, S. Bhattacharya, K. C. Barick, A. Guleria, K. Bhattacharyya, A. K. Yadav, A. Chakraborty, S. Rakshit, S. Patra, M. Lawande, S. Chakraborty and R. Chakravarty, ACS Applied Materials & Interfaces, 2025, 17, 42767-42780.
3. C. Mothé and M. Rao, Thermochimica acta, 2000, 357, 9-13.
4. P. Ramos and M. Broncel, Molecules, 2022, 27, 1510.
5. S. Latifi, K. Azzaoui, R. Sabbahi, G. Hanbali, B. Hammouti, M. Merzouki, M. M. Alanazi, S. F. Alshahateet, S. Jodeh and S. Saoiabi, Desalination and Water Treatment, 2025, 101272.
6. A. Watanabe, M. Kajita, J. Kim, A. Kanayama, K. Takahashi, T. Mashino and Y. Miyamoto, Nanotechnology, 2009, 20, 455105.
7. M. Farrag, Journal of Photochemistry and Photobiology A: Chemistry, 2016, 318, 42-50.
8. M. J. Hossain, M. Rahman and M. J. Sharif, Nanoscale Advances, 2020, 2, 1245-1252.
9. R. P. Charde, B. v. Devener and M. M. Nigra, Catalysts, 2023, 13, 246.
10. C. He, S. Sankarasubramanian, A. Ells, J. Parrondo, C. Gumeci, M. Kodali, I. Matanovic, A. K. Yadav, K. Bhattacharyya and N. Dale, ACS catalysis, 2021, 11, 7006-7017.
11. D. Tyagi, K. Scholz, S. Varma, K. Bhattacharya, S. Mali, P. Patil and S. Bharadwaj, international journal of hydrogen energy, 2012, 37, 3602-3611.
12. S. Mitra, A. Kumar, D. Tyagi, A. Sarkar, S. H. Rekapalli, M. D. Mukadam, A. Roy, D. Sen, K. Bhattacharyya and A. K. Tyagi, Nanoscale, 2026, 18, 843-867.
13. W. Wu, K. Bhattacharyya, K. Gray and E. Weitz, The Journal of Physical Chemistry C, 2013, 117, 20643-20655.

14. J. Grimblot, A. Luntz and D. Fowler, Journal of electron spectroscopy and related phenomena, 1990, 52, 161-174.
15. D. K. Roper, W. Ahn and M. Hoepfner, The Journal of Physical Chemistry C, 2007, 111, 3636-3641.
16. S. Ghosh, Y. Liang, W. Cai and R. Chakravarty, Journal of Nanobiotechnology, 2025, 23, 407.
17. S. Ghosh, D. Banerjee, A. Guleria and R. Chakravarty, Nuclear Medicine and Biology, 2024, 138-139, 108947.